Climate Dynamics (2026) 64:170
https://doi.org/10.1007/s00382-026-08145-9

ORIGINAL ARTICLE

Inter-basin teleconnections in the annual mean sea surface temperature field

Dazhi Zhang[1] · **Jianping Li**[1,2]

Received: 23 January 2026 / Accepted: 6 March 2026

Abstract
Inter-basin interactions are a pivotal driver of the global climate system. By employing the inter-basin teleconnectivity (IBT) analysis, this study systematically investigates the dominant simultaneous inter-basin linkages across the Pacific, Atlantic, and Indian Oceans in the annual mean sea surface temperature field. We identify 11 distinct inter-basin teleconnections (IBTs), which include two previously recognized patterns, i.e. the boundary current synchronization (BCS) and South Atlantic-South Indian Ocean synchronization (SASI), along with nine new potential IBTs. Two of these new IBTs respectively represent the inter-basin linkages of the Pacific Decadal Oscillation (PDO) and Indian Ocean Basin Mode (IOB) with other ocean basins. We mainly analyze the spatiotemporal characteristics of the remaining IBTs, namely the Bay of Bengal-South Atlantic synchronization (BBSA), Northwest Atlantic-Southeast Indian Ocean seesaw (NASI), Caribbean Sea-Southwest Indian Ocean seesaw (CSSI), Southwest Pacific-Southeast America synchronization (SPSA), North Pacific-South Atlantic seesaw (NPSA), North Tropical Indo-Pacific seesaw (NTIP), and Southern Hemispheric Tripole (SHT). The results demonstrate that these IBTs are statistically relatively independent of some known climate modes and exhibit distinct quasi-periodic characteristics on interannual to decadal timescales. These findings enhance our understanding about inter-basin linkages and interactions.

Keywords Inter-basin teleconnection (IBT) · Climate modes · Interannual variability · Decadal variability · Annual mean sea surface temperature

1 Introduction

Ocean–atmosphere interactions play a pivotal role in shaping and modulating the climate system (Gill 1982; Li et al. 2019a, b), giving rise to diverse climate modes. For example, in the Pacific Ocean, known climate modes include the El Niño-Southern Oscillation (ENSO), Pacific Decadal Oscillation (PDO), North Pacific Meridional Mode (NPMM), and South Pacific Meridional Mode (SPMM) (Bjerkenes 1969; Mantua et al. 1997; Chiang and Vimont 2004; Zhang et al. 2014). In the Indian Ocean, known climate modes include the Indian Ocean Basin Mode (IOB) and Indian Ocean Dipole Mode (IOD) (Klein et al. 1999; Saji et al. 1999). In the Atlantic Ocean, known climate modes include the Atlantic Niño, Atlantic Multidecadal Variability (AMV), North Tropical Atlantic (NTA) (Zebiak 1993; Kerr 2000; Czaja et al. 2002). These climate modes play distinct roles across various regions and exert substantial impacts on both society and the environment.

To advance our understanding on the impacts and mechanisms of distinct climate modes—and thereby improve climate predictability—researchers have increasingly focused on inter-basin interactions as a key driver of climate variability. Cai et al. (2019) systematically summarized previous research on pantropical inter-basin interactions. The three tropical oceans are connected through the Walker circulation, resulting in complex interactions. For example, the El Niño can lead to a decrease in surface evaporation and

✉ Jianping Li
ljp@ouc.edu.cn

[1] Frontiers Science Center for Deep Ocean Multi-Spheres and Earth System (DOMES)/Key Laboratory of Physical Oceanography/Academy of Future Ocean/College of Oceanic and Atmospheric Sciences/Center for Ocean Carbon Neutrality, Ocean University of China, Qingdao 266100, China

[2] Laboratory for Ocean Dynamics and Climate, Qingdao Marine Science and Technology Center, Qingdao 266237, China

Published online: 27 March 2026

an increase in downward shortwave radiation in the Indian Ocean through the Walker circulation (Klein et al. 1999), resulting in an IOB warming. The IOB warming, in turn, will accelerate the extinction of El Niño. Specifically, The IOB warming can lead to enhanced convection over the Indian Ocean, which in turn strengthens anomalous anticyclones in the northwest Pacific and easterly anomalies over the western equatorial Pacific, inhibiting the development of El Niño and even accelerating the phase transition from El Niño to La Niña (Izumo et al. 2016; Ha et al. 2017). In addition to interactions among the three tropical oceans, climatic connections also exist between high- and low-latitude regions across different ocean basins. Wang (2019) provides a comprehensive review of interactions between the principal modes of different ocean basins. For example, the sea surface temperature (SST) variability in the North Pacific exhibits a lagged response to AMV forcing by atmospheric teleconnections (Zhang and Delworth 2007).

Although considerable research has been conducted, previous studies have primarily focused on the interactions among major climate modes across different ocean basins. Can we develop a more universal perspective to understand and examine connections between different oceans? Han and Li (2023) developed an inter-basin teleconnectivity (IBT) analysis to investigate the dominant inter-basin teleconnections (IBTs) of the Indian Ocean with both the Pacific and Atlantic Oceans during boreal winter. Their analysis revealed a novel inter-basin climate mode, the Australian Boundary Current Dipole (ABCD), offering a new insight into the inter-basin interactions. However, their study primarily focused on negative correlations between ocean basins, and the IBTs between the Pacific and Atlantic Oceans were neglected. This study aims to systematically and comprehensively search for potential inter-basin linkages, including both positive and negative correlations, in the annual mean SST field using the IBT analysis. Through this approach, we identified the 11 strongest IBTs in the annual mean SST field, including two previously recognized IBTs and nine potentially new IBTs. These findings may strengthen the observational basis for inter-basin interactions across distinct basins.

The remainder of the paper is structured as follows. Section 2 provides a detailed account of the data and methodology used in this study. Section 3 presents the distribution characteristics of IBTs in the annual mean SST fields across the three major ocean basins. Section 4 discusses the spatiotemporal characteristics of IBTs between the Atlantic and the Indian Ocean. Section 5 discusses the spatiotemporal characteristics of IBTs between the Pacific and the Atlantic. Section 6 discusses the spatiotemporal characteristics of an IBT between the Pacific and the Indian Ocean. Section 7 discusses the spatiotemporal characteristics of an IBT across the three oceans in the Southern Hemisphere. Finally, Sect. 8 provides a summary and discussion.

2 Data and methods

2.1 Datasets

The SST data sets are obtained from two sources: (1) the National Oceanic and Atmospheric Administration (NOAA) Extended Reconstructed SST version 5 (ERSST v5) with a horizontal resolution of $2° \times 2°$ (Huang et al. 2017), and (2) the Japan Meteorological Agency's Centennial in situ Observation-Based Estimates SST (COBE SST) with a higher resolution of $1° \times 1°$ (Ishii et al. 2005). Both datasets cover the period from January 1950 to December 2022. The linear trend and long-term mean climatology have been removed from each data set. In the following analysis, grid points containing sea ice were masked and are represented by dark grey shading in the figures.

2.2 Indices

The El Niño–Southern Oscillation (ENSO) is represented by the Niño 3.4 index provided by the NOAA, defined as the area-averaged SST anomalies in the equatorial Pacific region (5°S–5°N, 170°–120°W). Eastern-Pacific (EP)-ENSO and Central-Pacific (CP)-ENSO are characterized by the E-index and C-index, respectively, which are obtained from a combination of the first two empirical orthogonal function (EOF) modes of SST anomalies over the equatorial Pacific (15°S–15°N, 140°E–80°W), each described by a spatial pattern and a principal component (PC) time series normalized to have a unit standard deviation (Takahashi et al. 2011; Geng et al. 2022). The E-Index is defined as $(PC1 - PC2)/\sqrt{2}$, and the C-Index is defined as $(PC1 + PC2)/\sqrt{2}$). The Pacific Decadal Oscillation (PDO) index is defined as the PC time series of the leading EOF mode of SST anomalies north of 20°N in the Pacific Ocean (Mantua et al. 1997). The South Pacific Meridional Mode (SPMM) index is calculated as the area- averaged SST anomalies over 25°–15°S, 90°–110°W (Zhang et al. 2014; Ding et al. 2020). The North Pacific Meridional Mode (NPMM) index is provided by the University of Wisconsin-Madison (Richter et al. 2022; https://www.aos.wisc.edu/dvimont/MModes/RealTime/PMM.txt). The Indian Ocean Basin (IOB) mode index is calculated as the area-averaged SST anomalies over 40°–110°E, 20°S–20°N (Yang et al. 2007; Zheng et al. 2011). The Indian Ocean Dipole (IOD) is represented by the Dipole Mode Index (DMI), defined as differences of SST anomalies averaged over the western (50°E–70°E; 10°S–10°N) and eastern (90°E–110°E;

10°S–0°) tropical Indian Ocean (Saji et al. 1999). The Atlantic Niño index is calculated as the area-averaged SST anomalies over 20°W–0°, 3°S–3°N (Zebiak 1993; Zhang and Han 2021). The Atlantic Multidecadal Variability (AMV) index is calculated as the area-averaged SST anomalies over 7.5°–75°W, 0°–60°N (Kerr 2000; Enfield et al. 2001; Sutton and Hodson 2005; Li et al. 2022). The North Tropical Atlantic (NTA) index is calculated as the area-averaged SST anomalies over 90°W–20°E, 0°–15°N (Ham et al. 2013). the SST Inter-Hemispheric Dipole (SSTID) index is calculated as the hemisphere–averaged SST anomalies in the northern hemisphere minus that in the southern hemisphere (Sun et al. 2013; An et al. 2024). The SAM index is defined as the difference in the normalized zonal-mean sea level pressure (SLP) between 40°S and 70°S (Nan and Li 2003).

2.3 IBT analysis

Unlike the atmosphere, which is highly interconnected, the oceans are separated by distinct boundaries. To find out IBTs between one specific ocean and the other oceans, Han and Li (2023) develop a new IBT analysis based on the teleconnectivity analysis (Wallace and Gutzler 1981). Kohyama et al. (2021b) proposed the Intensive Variability Extraction (IVE) method based on the principal component analysis (PCA), which reconstructs statistical degrees of freedom to extract interscale variability. Using this method, they discovered Boundary Current Synchronization (BCS) and Southern Hemispheric BCS. Although the IVE identify distant small-scale modes, it primarily focuses on a single ensemble to extract the dominant modes in that ensemble. In contrast, the IBT analysis focuses on two ensembles and aims to identify the strongest connections between them. The specific methodology is as follows:

All the grid points in one ocean basin are classified into Set A, and all the grid points in the other oceans are classified into Set B. After that, the cross-set correlation coefficients Rab (base point a in Set A, and every grid point b in Set B) between the grid points in Set A and all the grid points in Set B are calculated. Since the inter-basin connections could be characterized by negative and positive correlations, we could study the negative inter-basin teleconnectivity (nIBT) analysis and positive inter-basin teleconnectivity (pIBT) analysis based on the positive and negative orientation of Rab. Comparing the strongest positive or negative correlation on cross-set one-point correlation maps of different grids in the Set A contrast the strengths of teleconnection patterns in Set A. An IBT is defined as:

$$nIBT_a = max\left(|R_{ab}|\right) for\, all\, b, when\, R_{ab} < 0, a \in A, b \in B, \quad (1)$$

$$pIBT_a = max\left(R_{ab}\right) for\, all\, b, when\, R_{ab} > 0, a \in A, b \in B, \quad (2)$$

$$IBT_a = nIBT_a \bigcup pIBT_a. \quad (3)$$

To ensure the pIBT analysis captures truly remote linkages—rather than spurious local correlations near basin boundaries—we introduce a correlation radius for each grid point. Specifically, we first perform a pointwise correlation analysis between each grid point and all other global grid points to obtain the spatial correlation distribution. For each grid point, we then identified the largest connected region where correlation coefficients remained above 0.3, radiating outward from the original grid point. The farthest grid point X within this region was determined, and the distance between the original grid point and X is defined as the correlation radius for that location. During pIBT analysis, all grid points within this radius were excluded from consideration, ensuring that only statistically robust inter-basin linkages were retained in the final distribution.

Moreover, the IBT analysis not only considers simultaneous inter-basin connections, but also takes the lagged relationships into account. In this study, we focused on simultaneous IBT analysis.

2.4 Definition of the IBT index

To better analyze the spatiotemporal characteristics of each IBT, we define an index for each IBT. The negative dipole inter-basin teleconnection index (nIBTI) is defined as:

$$nIBTI = \frac{1}{2}([SSTA_{R1}] - [SSTA_{R2}]). \quad (4)$$

The positive bipolar inter-basin teleconnection index (pIBTI) is defined as:

$$pIBTI = \frac{1}{2}([SSTA_{R1}] + [SSTA_{R2}]), \quad (5)$$

where $SSTA_{R1}$ and $SSTA_{R2}$ represent the regional-mean SST anomalies over key regions R1 and R2. Details regarding the definition of key regions are provided in Text S1. The multipole inter-basin teleconnection index (mIBTI) is defined as:

$$mIBTI = \frac{1}{2i}\sum_{1}^{i}[SSTA_{pRi}] - \frac{1}{2j}\sum_{1}^{j}[SSTA_{nRj}], \quad (6)$$

where $SSTA_{pRi}$ and $SSTA_{nRj}$ represent the regional-mean SST anomalies over each positive pole (pRi) and negative pole (nRj). Details regarding the definition of 'multipole' are provided in Text S2.

2.5 Posteriori statistical test method

We use the spectral analysis posteriori statistical test method from Madden and Julian (1971) to examine the robustness of the identified IBTs. The posteriori sampling limit is established by setting the significance level to a point where it is highly unlikely for any estimates to exceed this limit. The method of estimating the spectra was that suggested by Bingham et al. (1967) which utilizes the fast Fourier transform (fFt). The algorithm makes use of the modified Fourier periodogram obtained by 1) removing the sample mean of the N members of the series, 2) "tapering" the first and last 10% of the resulting N members by multiplication by a segment of the cosine curve so that the ends of the series are zero, and 3) performing the fFt to obtain all N/2 harmonic coefficients. The squared amplitudes or modified periodogram estimates are then averaged by a running average of length L coefficients; this averaging produces spectrum an estimate of the continuous spectra viewed through a rectangular spectral window of bandwidth equal to $(2L/N)\, f_{Ny}$, where f_{Ny} is the Nyquist frequency.

In our analysis, we focus on IBT signals at interannual to decadal scales (2–20 years). Accordingly, the moving average length L is set to 3, resulting in a spectral window bandwidth of 0.041 year^{-1}. The number of independent spectral estimates q is 12 ($q \approx N/2L$). We select a prior level of 0.25%, implying an expectation of 0.03 estimates exceeding this level, with the posteriori confidence limit approximately at 3%.

2.6 Statistical methods

Statistical methods, such as the EOF analysis, continuous power spectrum, partial correlation and others, are used in this study.

3 Distribution of IBTs across the three oceans

Figure 1 presents the distribution of nIBTs and pIBTs among the three major oceans after removing the ENSO signal (Unless otherwise specified, the Niño 3.4 index is used to represent the ENSO signal.). The key regions of these IBTs are clearly identified, highlighting the primary areas where IBTs occur in the annual mean SST field. It is evident that each IBT key region is not an isolated single point but consists of a cluster of spatially aggregated grid cells, all of which maintain highly consistent correlation relationships with a specific region in another ocean basin (Fig. S4). This strongly demonstrates that the identified IBTs represent robust signals at the sea-area scale with good spatial representativeness, rather than coincidental point-to-point correlations. A comparison with the results retaining the ENSO signal (Fig. S5) demonstrates that ENSO's inter-basin influence on annual mean SST fields is primarily evident in the tropical Indian Ocean and equatorial Atlantic (Klein et al. 1999; Zhang et al. 2023), whereas its effect on the Indian Ocean-Atlantic Ocean teleconnection pattern is relatively limited. Notably, repeat experiments using different datasets (Fig. S6) yield consistent conclusions, confirming the robustness of the identified teleconnections and their independence from the choice of specific datasets.

As illustrated in Fig. 1a and d, the pIBTs between the Indian Ocean and the Atlantic are primarily manifested between the Indian Ocean and the South Atlantic, while the nIBTs are mainly manifested between the Indian Ocean and the North Atlantic. Five dominant IBTs are identified, including two positive modes: the Bay of Bengal (BOB)-South Atlantic synchronization (BBSA) and South Atlantic-South Indian Ocean synchronization (SASI), along with three negative modes: the North Atlantic-North Indian Ocean seesaw (NANI), Northwest Atlantic-Southeast Indian Ocean seesaw (NASI), and Caribbean Sea-Southwest Indian Ocean seesaw (CSSI). As illustrated in Fig. 1b and e, the pIBTs between the Pacific and Atlantic is primarily manifested between the western Pacific and the North Atlantic, while the nIBTs are mainly manifested between the eastern Pacific and the South Atlantic. Five dominant IBTs are identified, including three positive modes: the BCS, North Pacific-Mediterranean Sea synchronization (NPMS), and Southwest Pacific-Southeast Coast of America synchronization (SPSA), along with two negative modes: the North Pacific-South Atlantic seesaw (NPSA) and Tropical South Pacific-South Atlantic seesaw (TPSA). As illustrated in Fig. 1c and f, the pIBTs between the Indian Ocean and the Pacific are primarily manifested through the linkage between ENSO and the tropical Indian Ocean (Fig. S5), with weaker positive correlations observed in other regions. In contrast, two nIBTs are identified that operate independently of ENSO: the North Tropical Indo-Pacific seesaw (NTIP) and Tropical South Pacific-South Indian Ocean seesaw (TPSI).

Notably, Kohyama et al. (2021a) discovered and defined the BCS, which captures the inter-basin linkage between the Kuroshio and Gulf Stream. The Kuroshio and Gulf Stream exhibit synchronized variability, modulated by zonally symmetric atmospheric forcing over the Pacific and Atlantic basins, which leads to coherent SST anomalies (Kohyama et al. 2021a). Moreover, previous studies have noted the synchronous SST variability between the South Atlantic and South Indian Oceans, a feature that is well captured by the SASI pattern. Morioka et al. (2017) suggested that the South Atlantic may influence the South Indian Ocean via eastward-propagating oceanic Rossby waves. Additionally, Xue et al.

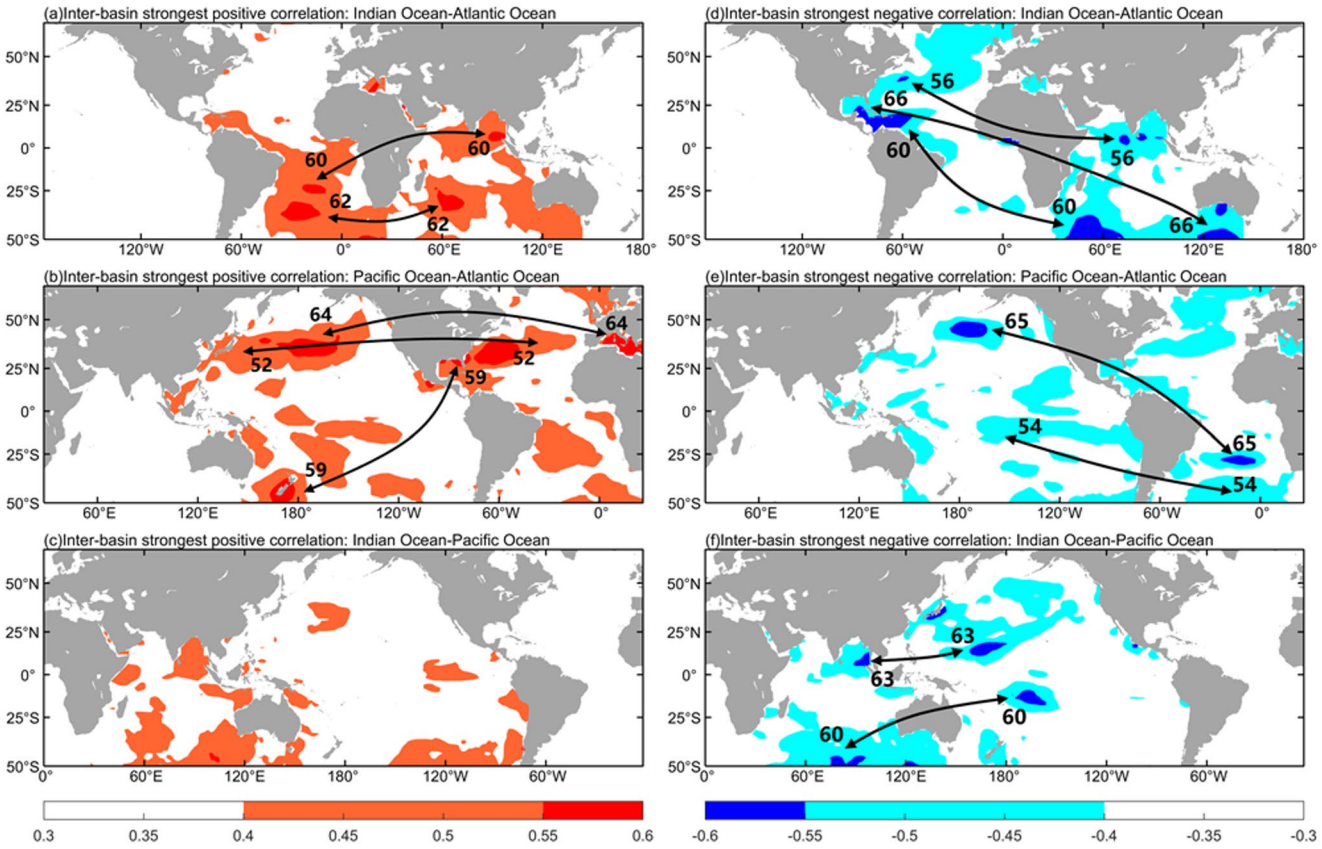

Fig. 1 Distribution of pIBTs in the annual mean SST field (1950–2022) after removing the ENSO signal. The correlation coefficients are multiplied by 100, and arrows connect the strongest positive teleconnection pairs. **a** Atlantic Ocean basin-Indian Ocean basin, **b** Pacific Ocean basin-Atlantic Ocean basin, **c** Indian Ocean basin-Pacific Ocean basin. Distribution of nIBTs in the annual mean SST field (1950–2022) after removing the ENSO signal. The negative signs are omitted, and the correlation coefficients are multiplied by 100. Arrows connect the strongest negative teleconnection pairs. **d** Atlantic Ocean basin-Indian Ocean basin, **e** Pacific Ocean basin-Atlantic Ocean basin, **f** Indian Ocean basin-Pacific Ocean basin. Based on ERSST v5

(2018a), through South Atlantic Pacemaker experiments, demonstrated that decadal variability in the South Atlantic can modulate atmospheric circulation, subsequently affecting surface wind speed and radiative fluxes over the South Indian Ocean and thereby influencing its SST. We have calculated the lead–lag correlation coefficients between the indices defined by our IBT analysis and the original mode indices defined by previous authors. As shown in Figures S7a and S8a, while there are some differences between the key sea areas we defined and those defined in the original studies (Kohyama et al. 2021a; Xue et al. 2018), they are very close, and both effectively represent the connection between the two ocean basins in these specific regions. The minor differences may be attributed to variations in the specific methods used to define the key sea areas and the differing resolutions of the datasets employed (Kohyama et al. 2021a). Furthermore, as illustrated in Figures S7b and S8b, the correlations between these indices consistently peak at the zero-lag (lag = 0) period and decay rapidly as the lead or lag time increases. These results demonstrate that the IBT analysis effectively captures previously identified IBTs, confirming its reliability.

3.1 Independence of IBTs in the annual mean SST field

As shown in Fig. 1, several IBTs exhibit spatial proximity or partial overlap between their key oceanic regions. Examples include the key regions of BBSA and NPSA in the South Atlantic (Fig. 1a, e), BBSA and NTIP in the northeastern Indian Ocean (Fig. 1a, f), and TPSA and TPSI in the tropical South Pacific (Fig. 1e, f). This raises the question of whether they represent the same IBT, thereby necessitating further discussion regarding their independence.

First, the key regions of NPSA and BBSA in the South Atlantic exhibit notable spatial proximity. However, the key region of BBSA in the South Atlantic is located further to the northwest, while that of NPSA is located further to the southeast. Partial correlation analysis (Fig. S9) reveals that after mutually removing each other's index signals, both of

them maintain statistically significant signals within their key regions, and the positions of the activity centers exhibit no substantial change. Therefore, we suggest that NPSA and BBSA represent relatively independent IBTs. Similarly, BBSA and NTIP show clear regional differences in their key regions of the northeastern Indian Ocean: the former is concentrated in the BOB, while the latter is located in the Andaman Sea, Gulf of Thailand, and southern South China Sea. Fig. S10 shows that after mutually removing each other's index signals, significant signals persist in their respective key regions, with no substantial change in the centers of action, further supporting their independence.

In contrast, TPSI and TPSA exhibit closely overlapping key regions in the tropical South Pacific. The partial correlation analysis (Fig. S11) indicates that, after mutual signal removal, the signals within their key regions in the tropical South Pacific exhibit a significant reduction in strength, along with a substantial displacement of the action centers from their original regions. Does this suggest that TPSI and TPSA fundamentally represent a single IBT? Fig. S12 presents the first two EOF modes of annual mean SST over the Southern Hemisphere (0°-50°S), including their spatial patterns and PC time series. Both modes satisfy the North's test (North et al. 1982). The leading EOF mode (EOF1) captures a spatial pattern characteristic of the ENSO, accounting for 30.4% of the total variance in the hemispheric SST field. The PC1 time series exhibits a high correlation coefficient of 0.90 with the Niño3.4 index, confirming that EOF1 in fact reflects the ENSO signature in Southern Hemisphere SST variability. The second mode (EOF2), accounting for 10.4% of the total variance, reveals an inter-basin tripole pattern across the three major ocean basins characterized by: negative (positive) SST anomalies in the mid-latitude South Atlantic and South Indian Oceans and positive (negative) SST anomalies in the tropical south Pacific. Therefore, we suggest that TPSA and TPSI essentially represent the same IBT, which we term the Southern Hemispheric Tripole (SHT).

3.2 Comparison of IBTs with several known modes

To determine whether the IBTs identified via the IBT analysis reflect the inter-basin effects of known oceanic modes, we calculate correlation coefficients between the nine identified IBTs indices (excluding BCS and SASI) and several known modes indices (Table 1). Notably, NANI shows a significant positive correlation with the IOB mode (r = 0.84), while the NPMS shows a significant negative correlation with the PDO (r = -0.85). Fig. S13 presents the partial correlation maps of NANI after removing the signals of the IOB mode. We can observe that the signal of NANI in the North Indian Ocean has significantly weakened. Fig. S14 presents the partial correlation maps of the NPMS after removing the signals of the PDO. We can observe that the signal of NPMS in the North Pacific Ocean has also decreased and the activity center has changed significantly. Therefore, we suggest that NANI may reflect the linkage between the IOB mode and the North Atlantic, and that NPMS may reflect the linkage between the PDO and the Mediterranean Sea. Regarding the remaining seven IBTs, we also identified statistically significant correlations with several known oceanic modes. These relationships will be discussed in subsequent sections.

4 IBTs between the Atlantic Ocean basin and Indian Ocean basin

4.1 BBSA

Figure 2a and b show the regional correlation maps between the global SST anomalies and regional mean SST anomalies in the two key regions of BBSA. The key regions (black boxes) are located in the BOB (82°–100°E, 4°–12°N) and the South Tropical Atlantic (8°–28°W, 18°–26°S). Figure 2c presents the normalized SST time series for these two key oceanic regions. A pronounced in-phase relationship is evident between them, with a correlation coefficient of 0.56. Figure 2d illustrates the spatial structure of BBSA. Specifically, during positive BBSA events, the Bay of Bengal

Table 1 The temporal correlation matrix for the IBTs indices and several known oceanic modes indices

	PDO	NPMM	SPMM	IOB	IOD	AMV	Atlantic Niño	NTA	SSTID
BBSA	0.39*	−0.01	0.31*	0.67*	0.02	−0.31*	0.23	0.09	−0.55*
NANI	0.47*	0.06	0.37*	0.84*	0.18	0.43*	0.17	0.08	−0.55*
NASI	−0.01	0.20	−0.09	−0.27	−0.10	0.48*	−0.17	−0.12	0.65*
CSSI	−0.03	0.17	0.00	0.21	−0.10	0.33*	0.03	0.49*	0.41*
NPMS	−0.85*	−0.16	0.57*	−0.39*	0.03	0.23	−0.09	0.03	0.58*
SPSA	−0.42*	−0.10	−0.38*	−0.39*	−0.04	0.00	0.08	0.31*	0.14
NPSA	−0.57*	0.01	−0.40*	−0.45*	0.06	0.17	−0.15	−0.03	0.55*
NTIP	0.35*	−0.18	0.30*	0.59*	−0.16	−0.17	0.01	−0.08	−0.45*
SHT	0.15	0.38*	0.15	0.14	−0.01	0.34*	−0.08	−0.23	0.40*

The asterisks indicate significant values at the 99% confidence level

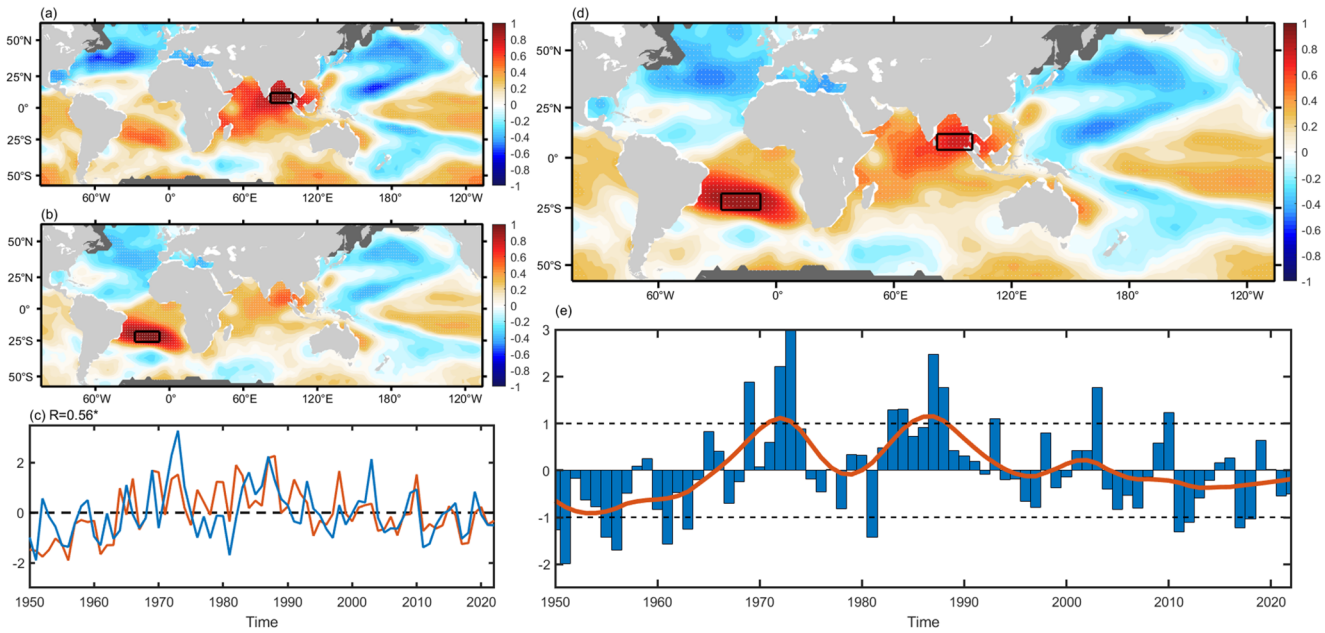

Fig. 2 **a** Regional correlation maps between global SST anomalies and regional-mean SST anomalies in the BOB (82°–100°E, 4°–12°N). **b** in the tropical South Atlantic (8°–28°W, 18°–26°S). Dots indicate the correlations significant at the 99% confidence level. **c** Time series of annual mean SST anomalies for the two regions, with the blue line representing the BOB (boxed region in **a**) and the red line representing the Tropical South Atlantic (boxed region in **b**). **d** Correlation map between the BBSA index and the global SST anomalies. **e** Bar plot of the standardized BBSA index, with the red line representing the 7-year lowpass filtered value

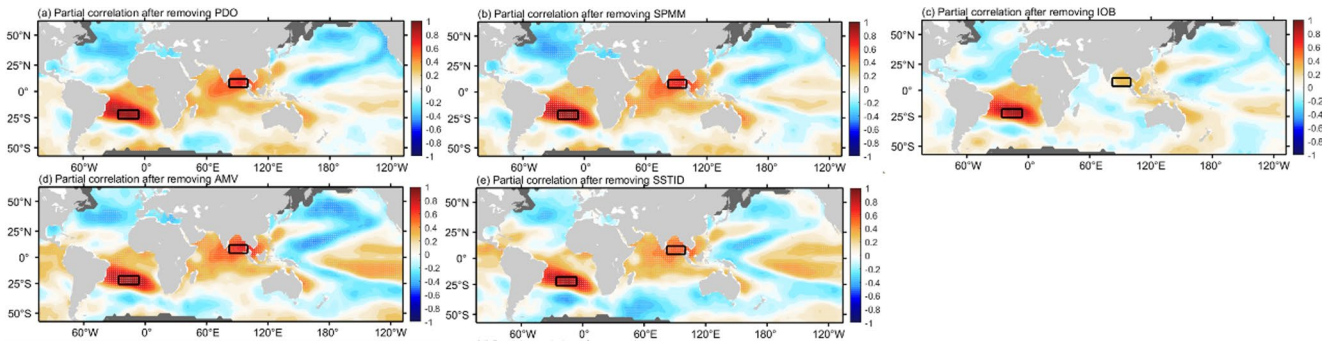

Fig. 3 Partial correlation maps between the global SST anomalies and BBSA index after removing the signals of several known modes. **a** PDO. **b** SPMM **c** IOB **d** AMV **e** SSTID. Dots indicate the correlations significant at the 99% confidence level

exhibits pronounced positive SST anomalies, accompanied by synchronous warming in the South Tropical Atlantic. Notably, the entire tropical Indian Ocean exhibits coherent variability; however, as illustrated in Fig. 2b, the South Tropical Atlantic shows the strongest correlation specifically with the BOB, indicating region-specific SST variability in the BOB itself. In the Northern Hemisphere, both the mid-latitude North Atlantic and North Pacific exhibit SST anomalies cooling. Figure 2e presents the normalized BBSA index time series. Based on power spectral analysis, we find that BBSA has quasi-periodic characteristics with a period of approximately 3–5 years on interannual scales (Fig. S15a). While on decadal scales, BBSA exhibits quasi-periodic characteristics with a period of approximately 10–20 years (Fig. S16a).

Table 1 reveals significant correlations between BBSA and several known modes, including PDO, SPMM, IOB, AMV and SSTID. For example, BBSA exhibits a positive correlation with the IOB, which is reasonable in view of the fact that the IOB represents the dominant mode of SST variability in the Tropical Indian Ocean, and the key region in the Indian Ocean of BBSA overlaps with the action center of the IOB. Figure 3 presents the partial correlation maps of BBSA after removing the signals of these known modes. Notably, after removing the IOB index, which encompasses the entire tropical Indian Ocean SST signal, the western Indian Ocean correlation reverses from positive to negative.

While the BOB signal weakens moderately, it remains statistically significant with minimal spatial displacement of its center of action. This suggests that although the BBSA is largely influenced by the IOB mode, there remains a component relatively independent of the IOB, and it is not entirely driven by the IOB mode. Similarly, the removal of other mode indices does not lead to major changes in the signals over these two key regions. These results indicate BBSA is distinct from these modes and exists as a relatively independent IBT.

4.2 NASI

Figure 4a and b show the regional correlation maps between the global SST anomalies and regional mean SST anomalies in the two key regions of NASI. The key regions (black boxes) are located in the Northwestern Atlantic extending from the Apalachee Bay southward to the Cayman Islands (74°–90°W, 14°–32°N) and the Southeastern Indian Ocean south of Australia (118°–134°E, 32°–50°S). These two regions exhibit an inter-hemispheric and inter-basin seesaw-like pattern in SST anomalies. Figure 4c presents the normalized SST time series for these two key oceanic regions. A pronounced anti-phase relationship is evident between them, with a correlation coefficient of − 0.56. Figure 4d illustrates the spatial structure of NASI. Specifically, during positive NASI events, the Northwestern Atlantic exhibits pronounced positive SST anomalies, concurrent with negative SST anomalies in the Southeastern Indian Ocean. Furthermore, beyond these two local regions, SST anomalies across the global oceans exhibit an antisymmetric pattern relative to the equator, particularly pronounced in the Atlantic—a spatial signature resembling that of SSTID (Sun et al. 2013; An et al. 2024). Moreover, significant cooling SST anomalies are observed in the Agulhas Current region off the southeastern coast of South Africa. Figure 4e presents the normalized NASI index time series. Based on power spectral analysis, we find that NASI has quasi-periodic characteristics with a period of approximately 2–4 years on interannual scales (Fig. S15b). On decadal scales, NASI exhibits quasi-periodic characteristics with a period of approximately 10–25 years (Fig. S16b). Its quasi-periodicity likely extends over a broader range, potentially limited by the study period. It exhibits phased behavior, with NASI transitioning from a positive to a negative phase around 1965 and from a negative back to a positive phase around 2015, displaying a "negative-positive-negative" pattern over the study period.

Table 1 reveals significant correlations between NASI and both the AMV and the SSTID. Figure 5 presents the partial correlation maps of NASI after removing the AMV and SSTID signals. Notably, NASIS signal remains statistically significant in the northwestern Atlantic key region even after removing the AMV signal, which captures basin-scale North Atlantic SST variability. Removal of the SSTID signal eliminates the interhemispheric antisymmetric SST pattern while preserving significant signals within the two

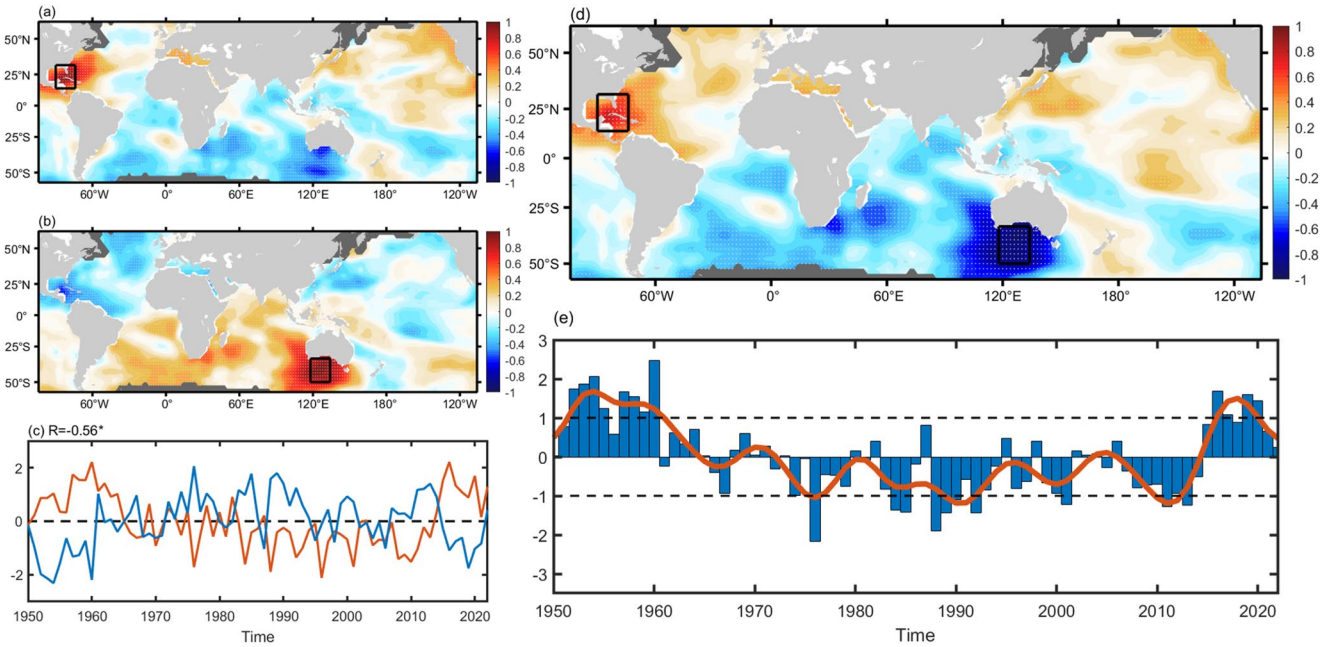

Fig. 4 As in Fig. 2, but **a** in the northwestern Atlantic (74°–90°W, 14°–32°N). **b** in the southeastern Indian Ocean (118°–134°E, 32°–50°S). **c** blue line representing the northwestern Atlantic (boxed region in **a** and the red line representing the southeastern Indian Ocean (boxed region in **b**). **d** between the NASI index and the global SST anomalies. **e** of the standardized NASI index

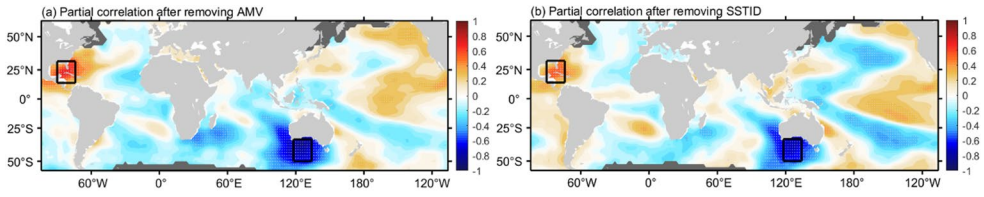

Fig. 5 Partial correlation maps between the global SST anomalies and NASIS index after removing the signals of several known modes. **a** AMV. **b** SSTID. Dots indicate the correlations significant at the 99% confidence level

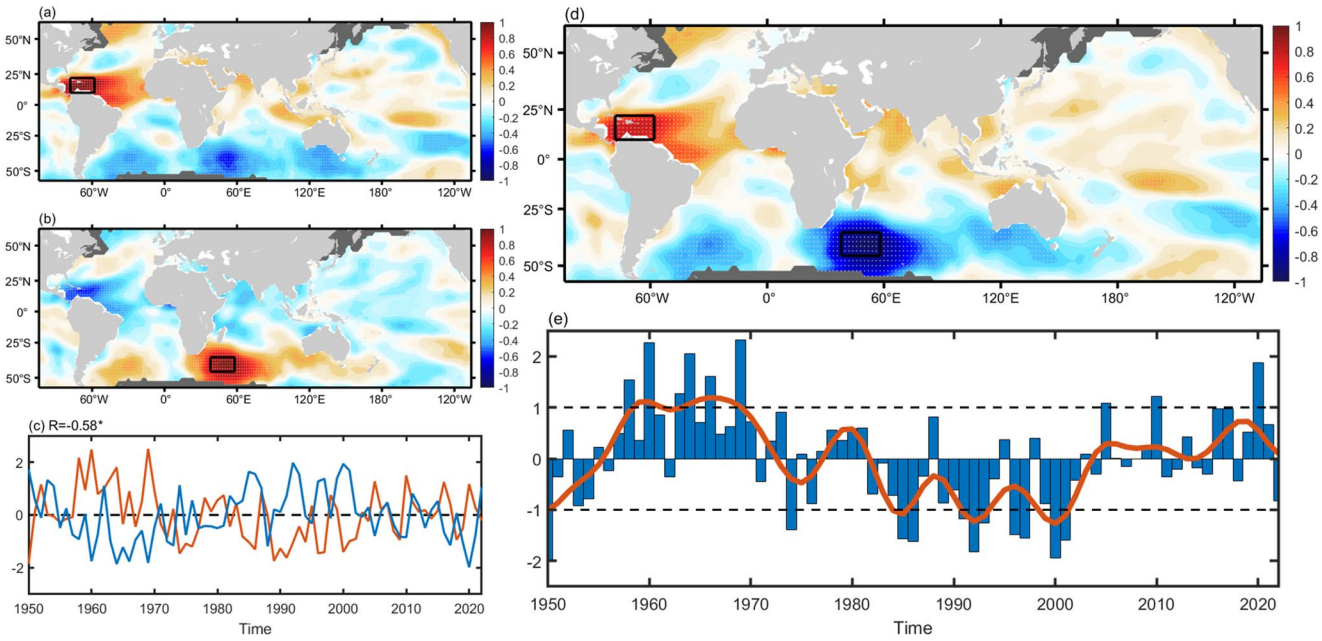

Fig. 6 As in Fig. 2, but **a** in the Caribbean Sea (58°–78°W, 10°–22°N). **b** in the southwestern Indian Ocean (38°–58°E, 36°–46°S). **c** blue line representing the Caribbean Sea (boxed region in **a**) and the red line representing the southwestern Indian Ocean (boxed region in **b**). **d** between the CSSI index and the global SST anomalies. **e** of the standardized CSSI index

key regions. These results indicate that NASI is distinct from these modes and exists as a relatively independent IBT.

4.3 CSSI

Figures 6a and b show the regional correlation maps between the global SST anomalies and regional mean SST anomalies in the two key regions of CSSI. The key regions (black boxes) are located in the Caribbean Sea (58°–78°W, 10°–22°N) and the mid-latitude Southwestern Indian Ocean (38°–58°E, 36°–46°S). These two regions exhibit an inter-basin seesaw-like pattern in SST anomalies. Figure 6c presents the normalized SST time series for these two key oceanic regions. A pronounced anti-phase relationship is evident between them, with a correlation coefficient of −0.58. Figure 6d illustrates the spatial structure of CSSI. Specifically, during positive CSSI events, the Caribbean Sea exhibits pronounced positive SST anomalies, concurrent with negative SST anomalies in the Southwestern Indian Ocean. Additionally, significant warming SST anomalies are observed in the northeastern Brazilian coast and the Gulf of Guinea. Moreover, the South Atlantic Ocean exhibits colder SST anomalies, which may be attributed to its covariability with the South Indian Ocean (Fig. 1a). Figure 6e presents the normalized CSSI index time series. Based on power spectral analysis, we find that CSSI has quasi-periodic characteristics with a period of approximately 3–4 years on interannual scales (Fig. S15c). On decadal scales, CSSI exhibits quasi-periodic characteristics with a period of approximately 10–15 years (Fig. S16c). It also exhibits phased behavior, with CSSI transitioning from a negative to a positive phase around 1955 and 2005, and from a positive back to a negative phase around 1980, displaying a "negative-positive-negative-positive" pattern over the study period.

Table 1 reveals significant correlations between CSSI and three known modes, including AMV, NTA and SSTID. For example, CSSI exhibits a positive correlation with the NTA, which is reasonable in view of the fact that the NTA represents the dominant mode of SST variability in the North Tropical Atlantic, and the key region in the North Atlantic of CSSI overlaps with the action center of the NTA. Figure 7 presents the partial correlation maps of CSSI after removing the signals of these known modes. The two key regions maintain robust signals without significant spatial

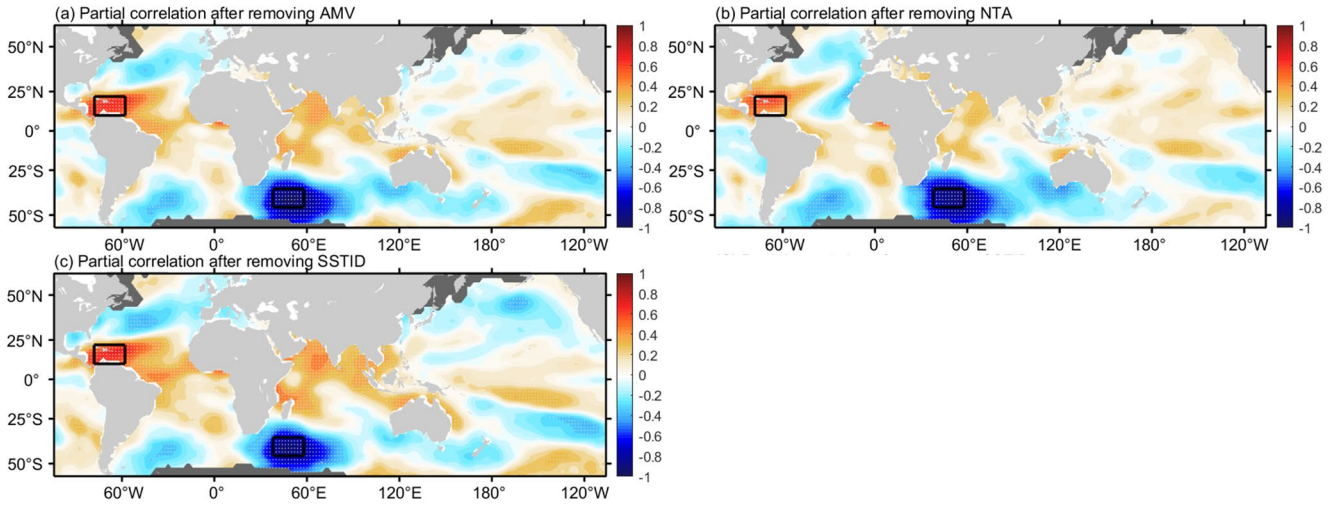

Fig. 7 Partial correlation maps between the global SST anomalies and CSSI index after removing the signals of several known modes. **a** AMV. **b** NTA. **c** SSTID. Dots indicate the correlations significant at the 99% confidence level

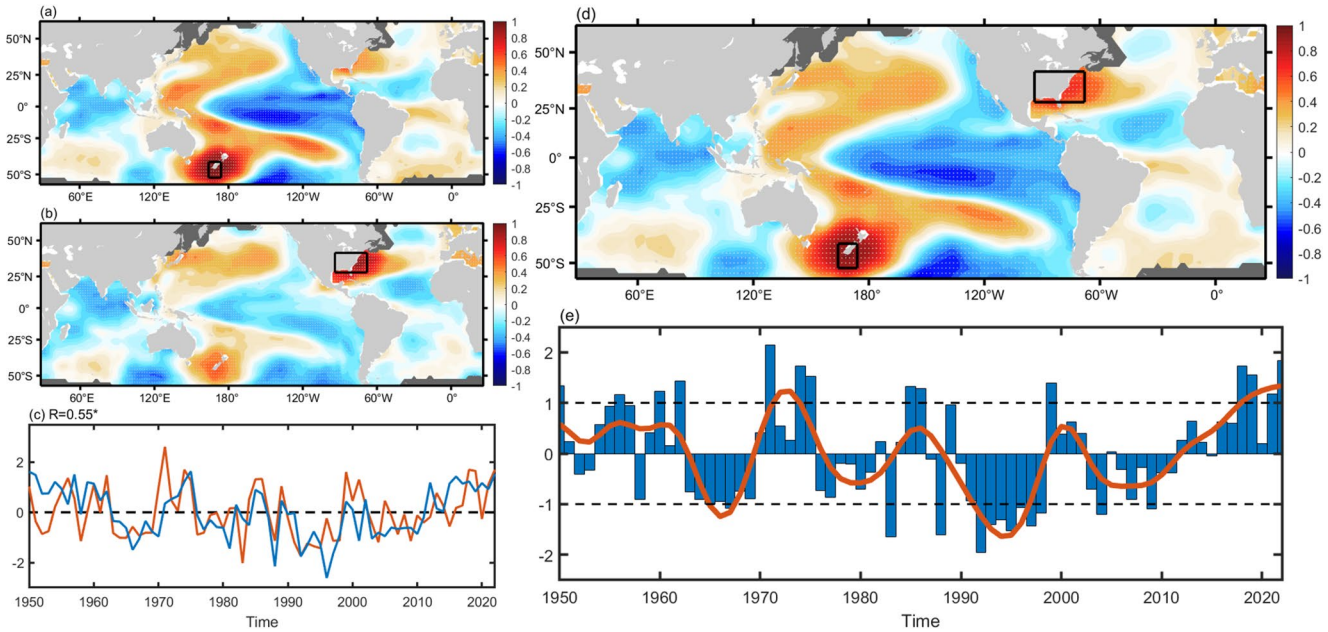

Fig. 8 As in Fig. 2, but **a** in the Southwest Pacific region (164°–174°E, 42°–52°S). **b** in the southeastern coast of North America (68°–94°W, 28°–42°N). **c** blue line representing the Southwest Pacific (boxed region in **a**) and the red line representing the southeastern coast of North America (boxed region in **b**). **d** between the SPSA index and the global SST anomalies. **e** of the standardized SPSA index

shifts, indicating that CSSI is distinct from these modes and exists as a relatively independent IBT.

5 IBTs between the Pacific Ocean basin and Atlantic Ocean basin

5.1 SPSA

Figures 8a and b show the regional correlation maps between the global SST anomalies and regional mean SST anomalies in the two key regions of SPSA. The key regions (black boxes) are located in the Southwest Pacific near New Zealand (164°–174°E, 42°–52°S) and the southeastern coast of North America (68°–94°W, 28°–42°N). We observe that while the southwestern Pacific exhibits strong internal correlations within the South Pacific basin, the strongest positive inter-basin correlation exists between the southwestern Pacific and the southeastern coast of North America in the North Atlantic. Conversely, this latter region shows a strong positive correlation solely with the southwestern Pacific. Figure 8c presents the normalized SST time series for these

two key oceanic regions. A pronounced in-phase relationship is evident between them, with a correlation coefficient of 0.55. Figure 8d illustrates the spatial structure of SPSA. Specifically, during positive SPSA events, the Southwest Pacific exhibits pronounced positive SST anomalies, accompanied by synchronous warming in southeastern coast of North America. Additionally, the South Pacific exhibits a meridional tripole SST pattern, while the North Pacific displays a zonal horseshoe-like mode. The tropical Indian Ocean and tropical North Atlantic both feature cooling SST anomalies. However, the South Atlantic demonstrates a weak correlation with SPSA. Figure 8e presents the normalized SPSA index time series. Based on power spectral analysis, we find that SPSA has quasi-periodic characteristics with a period of approximately 4–5 years on interannual scales (Fig. S15d). On decadal scales, SPSA exhibits several phase transitions between 1950 and 2022, characterized by a quasi-periodicity of approximately 16 years (Fig. S16d).

Table 1 reveals significant correlations between SPSA and several known modes, including PDO, SPMM, IOB and NTA. Figure 9 presents the partial correlation maps of SPSA after removing the signals of these known modes. Notably, the two key regions maintain robust signals without significant spatial displacement. Particularly striking is the persistence of significant signals in the Southwest Pacific near New Zealand after removing both PDO and SPMM influences, while other Pacific regions show diminished correlations. These results indicate that SPSA is distinct from these modes and exists as a relatively independent IBT.

5.2 NPSA

Figures 10a and b show the regional correlation maps between the global SST anomalies and regional mean SST anomalies in the two key regions of NPSA. The key regions (black boxes) are located in the central mid-latitude North Pacific (178°E–162°W, 40°–50°N) and the central subtropical South Atlantic (6°–26°W, 34°–24°S). These two regions exhibit an inter-hemispheric and inter-basin seesaw-like pattern in SST anomalies. Figure 10c presents the normalized SST time series for these two key oceanic regions. A pronounced anti-phase relationship is evident between them, with a correlation coefficient of −0.62. Figure 10d illustrates the spatial structure of NPSA. Specifically, during positive NPSA events, the mid-latitude North Pacific exhibits pronounced positive SST anomalies, concurrent with negative SST anomalies in the subtropical South Atlantic. Moreover, significant cooling SST anomalies are observed in the Gulf of Thailand, the Karimata Strait, and the southern South China Sea. In the South Pacific, SST anomalies display a northeast-southwest meridional dipole pattern. In the North Atlantic, however, NPSA does not exhibit a significant correlation with SST anomalies, even though studies have suggested the existence of decadal-scale linkages between SST variability in the North Atlantic and the North Pacific (Zhang & Delworth 2007; Wang 2019; Kohyama et al. 2021a). Figure 10e presents the normalized NPSA index time series. Based on power spectral analysis, we find that NPSA has quasi-periodic characteristics with a period of approximately 2–7 years on interannual scales (Fig. S15e). While on decadal scales, NPSA exhibits quasi-periodic characteristics with a period of approximately 10–14 years (Fig. S16e).

Table 1 reveals significant correlations between NPSA and several known modes, including PDO, SPMM, IOB and SSTID. For example, NPSA exhibits a negative correlation with the PDO, which is reasonable in view of the fact that the PDO represents the dominant mode of SST variability

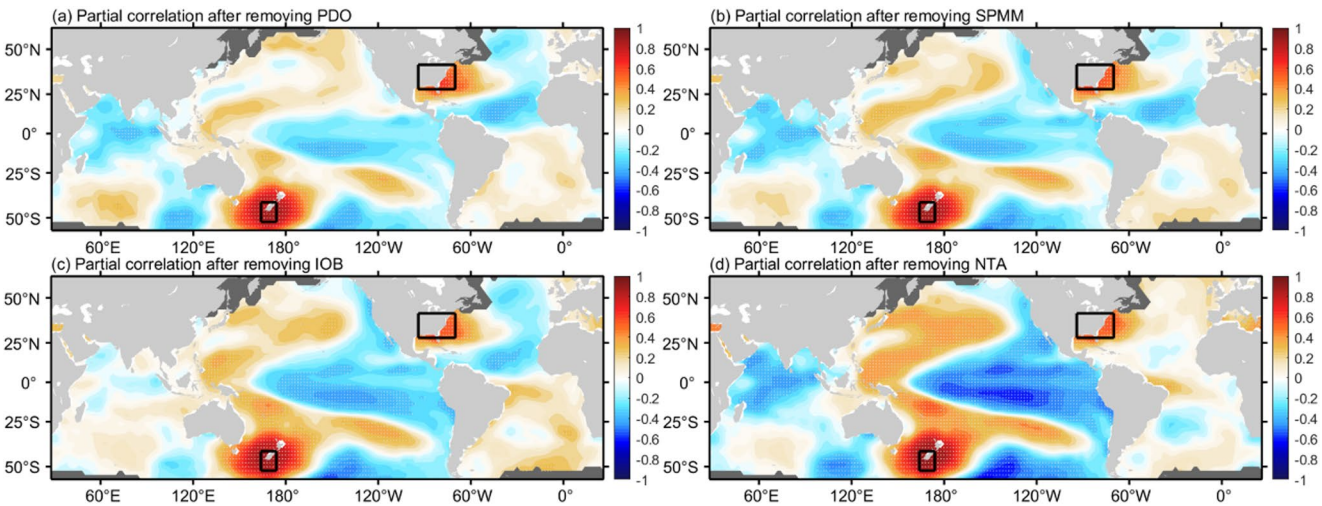

Fig. 9 Partial correlation maps between the global SST anomalies and SPSA index after removing the signals of several known modes. **a** PDO. **b** SPMM. **c** IOB. **d** NTA. Dots indicate the correlations significant at the 99% confidence level

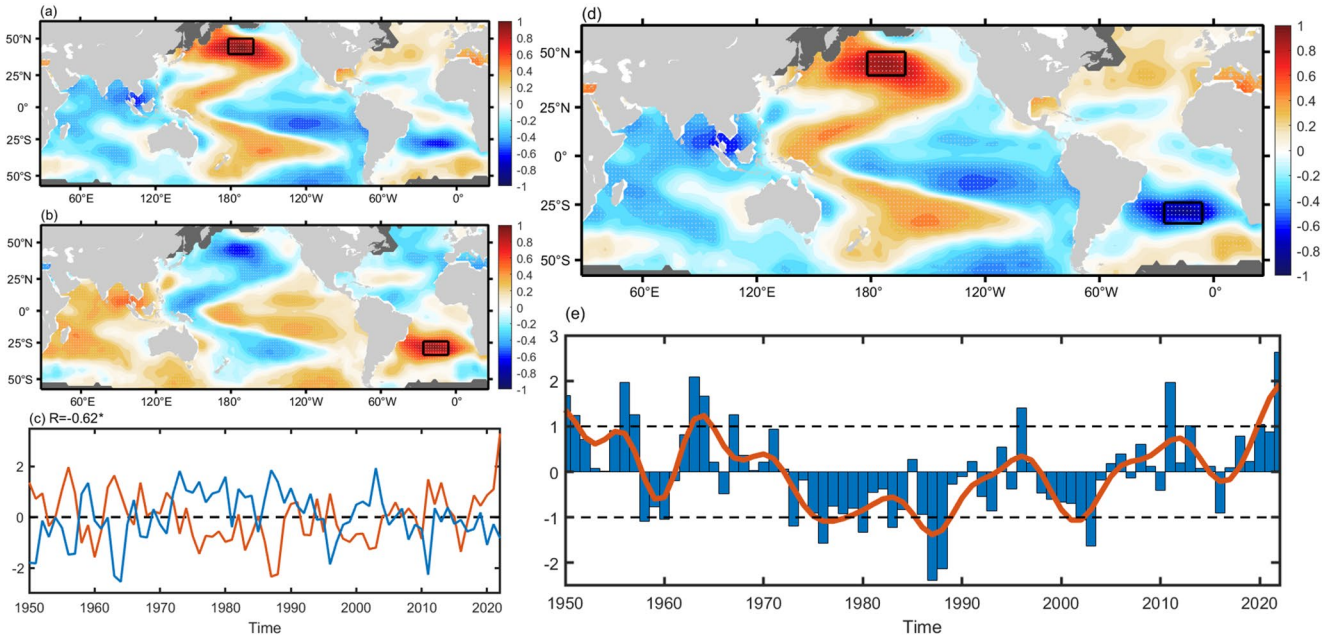

Fig. 10 As in Fig. 2, but **a** in the North Pacific region (178°E-162°W, 40°-50°N). **b** in the South Atlantic region (6°-26°W, 24°-34°S). **c** blue line representing the North Pacific (boxed region in **a**) and the red line representing the South Atlantic (boxed region in **b**). **d** between the NPSA index and the global SST anomalies. **e** of the standardized NPSA index

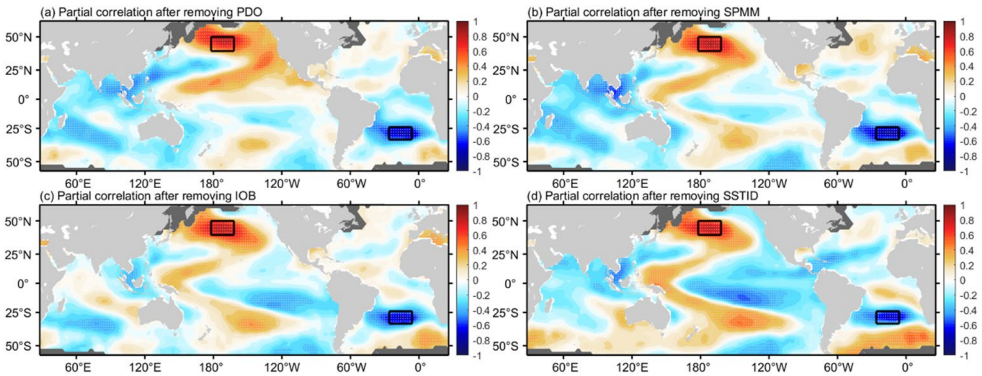

Fig. 11 Partial correlation maps between the global SST anomalies and NPSA index after removing the signals of several known modes. **a** PDO. **b** SPMM. **c** IOB. **d** SSTID. Dots indicate the correlations significant at the 99% confidence level

in the North Pacific, and the key region in the North Pacific of NPSA overlaps with the action center of the PDO. Figure 11 presents the partial correlation maps of NPSA after removing the signals of these known modes. The two key regions maintain robust signals without significant spatial shifts, indicating that NPSA is distinct from these modes and exists as a relatively independent IBT.

6 An IBT between the Indian Ocean basin and Pacific Ocean basin: NTIP

Figure 12a and b show the regional correlation maps between the global SST anomalies and regional mean SST anomalies in the two key regions of NTIP. The key regions (black boxes) are located in the Indo-Pacific sector encompassing the Andaman Sea, the Gulf of Thailand, and the southern South China Sea (94°–112°E, 0°–14°N), and the Tropical Northwestern Pacific (158°–176°E, 10°–20°N). These two regions exhibit an inter-basin seesaw-like pattern in SST anomalies. Figure 12c presents the normalized SST time series for these two key oceanic regions. A pronounced anti-phase relationship is evident between them, with a correlation coefficient of -0.60. Figure 12d illustrates the spatial structure of NTIP. Specifically, during positive NTIP events, the Indo-Pacific sector exhibits pronounced positive SST anomalies, concurrent with negative SST anomalies in the Tropical Northwestern Pacific. The Indo-Pacific signal extends northeastward into the South China Sea and the Philippine Sea, while the tropical northwestern Pacific signal exhibits a southwest–northeast orientation. Notably, an anticyclonic system—the Western Pacific Subtropical High (WPSH)—overhangs the two key NTIP regions, suggesting a potential interaction between NTIP and the

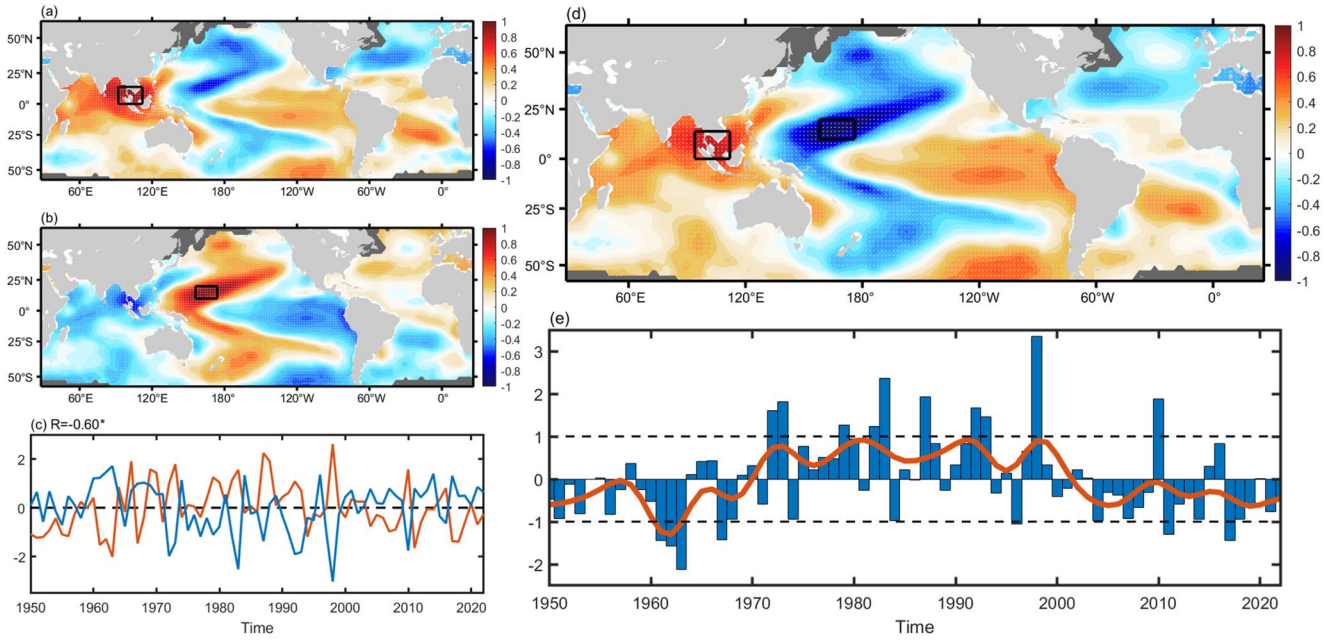

Fig. 12 As in Fig. 2, but **a** in the Indo-Pacific sector (94°–112°E, 0°–14°N). **b** in the tropical northwestern Pacific (158°–176°E, 10°–20°N). **c** blue line representing the Indo-Pacific sector (boxed region in **a**) and the red line representing the tropical northwestern Pacific (boxed region in **b**). **d** between the NTIP index and the global SST anomalies. **e** of the standardized NTIP index

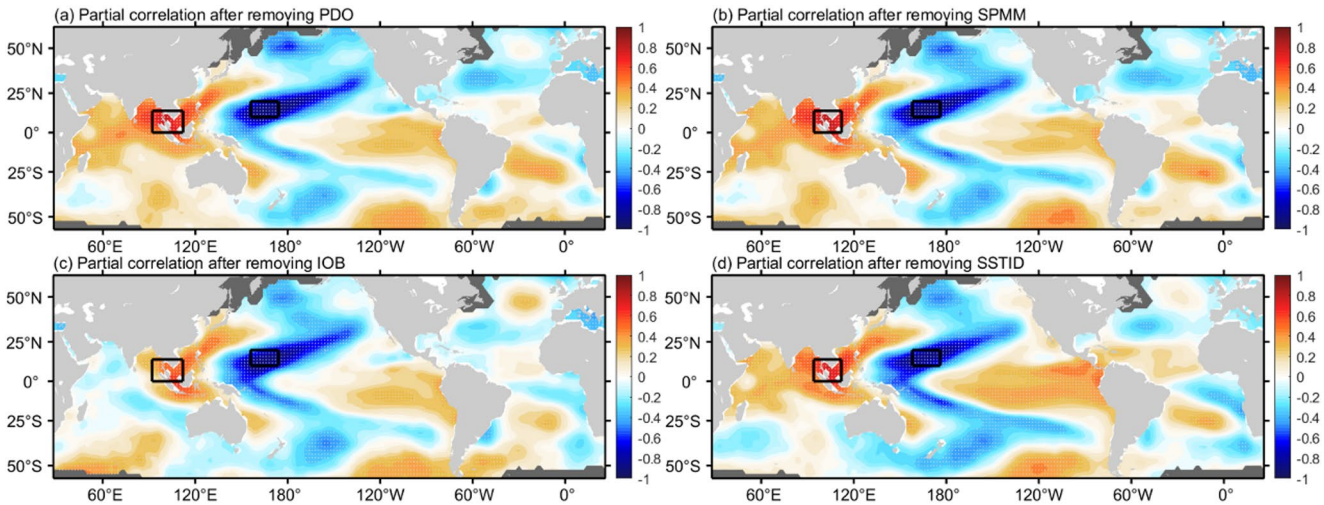

Fig. 13 Partial correlation maps between the global SST anomalies and NTIP index after removing the signals of several known modes. **a** PDO. **b** SPMM **c** IOB **d** SSTID. Dots indicate the correlations significant at the 99% confidence level

WPSH (Wang et al. 2013). The tropical Pacific exhibits an ENSO-like pattern; however, even after removing the ENSO signal, the IBT continues to detect NTIP, indicating that the connection between these two oceanic regions is independent of ENSO. Additionally, a pronounced cooling is observed in the SST in the western mid-latitude North Pacific. In the Atlantic basin, the mid-latitude North Atlantic and the subtropical South Atlantic exhibit a meridional dipole pattern. Figure 12e presents the normalized NTIP index time series. Based on power spectral analysis, we find that NTIP has quasi-periodic characteristics with a period of approximately 2–5 years on interannual scales (Fig. S15f). On decadal scales, NTIP exhibits quasi-periodic characteristics of approximately 10 years (Fig. S16f). It also exhibits phased behavior, with NTIP transitioning from a positive to a negative phase around 1970, and from a negative back to a positive phase around 2000, displaying a "negative-positive-negative" pattern over the study period.

Table 1 reveals significant correlations between NTIP and several modes, including PDO, SPMM, IOB and SSTID. Figure 13 presents the partial correlation maps of NTIP after removing the signals of these known modes. Notably, after

removing the IOB index, as with the BBSA, the western Indian Ocean correlation reverses from positive to negative. While the Indo-Pacific sector signal weakens moderately, it remains statistically significant with minimal spatial displacement of its center of action. Similarly, the removal of other mode indices does not lead to major changes in the signals over these two key regions. These results indicate that NTIP is distinct from these modes and exists as a relatively independent IBT.

7 An IBT across the three ocean basins in the Southern Hemisphere: SHT

The IBT analysis results reveal a significant negative correlation between the tropical South Pacific and both the South Indian and South Atlantic Oceans. EOF analysis further indicates that EOF2 mode of Southern Hemispheric SST effectively captures this inter-basin relationship. By integrating the IBT and EOF analyses, we select three key regions (Fig. S12c) to construct the SHT index: the mid-latitude South Indian Ocean (8°–30°E, 34°–50°S), the Tropical South Pacific (154°–166°W, 10°–16°S), and the mid-latitude South Atlantic (60°–80°W, 32°–50°S). The index exhibits a strong correlation (r = 0.81) with the PC2 time series, confirming its robust representation of SHT. Figure 14a and b show the regional correlation maps between the global SST anomalies and regional mean SST anomalies in the three key regions of SHT. Each region exhibits statistically significant correlation patterns with the other two basins, characterized by anti-phase variability between the tropical South Pacific and South Indian Ocean (r = −0.41), in-phase variability between the South Indian and South Atlantic Oceans (r = 0.41), and anti-phase variability between the tropical South Pacific and South Atlantic (r = − 0.42), further validating the robustness of the SHT definition. Figure 14d illustrates the spatial structure of SHT. Specifically, during positive SHT events, the Tropical South Pacific exhibits pronounced positive SST anomalies, concurrent with negative SST anomalies in the South Atlantic and South Indian Ocean. Additionally, warming signals are observed in the central-eastern tropical Pacific and the Atlantic Warm Pool region. Figure 14e presents the normalized SHT index time series. Based on power spectral analysis, we find that SHT has quasi-periodic characteristics with a period of approximately 3–4 years on interannual scales (Fig. S15g). On decadal scales, SHT exhibits quasi-periodic characteristics with a period of approximately 10–16 years (Fig. S16g). During the study period, SHT exhibits distinct phased characteristics before and after the 1990s. Between 1950 and 1990, SHT shifted from a positive to a negative

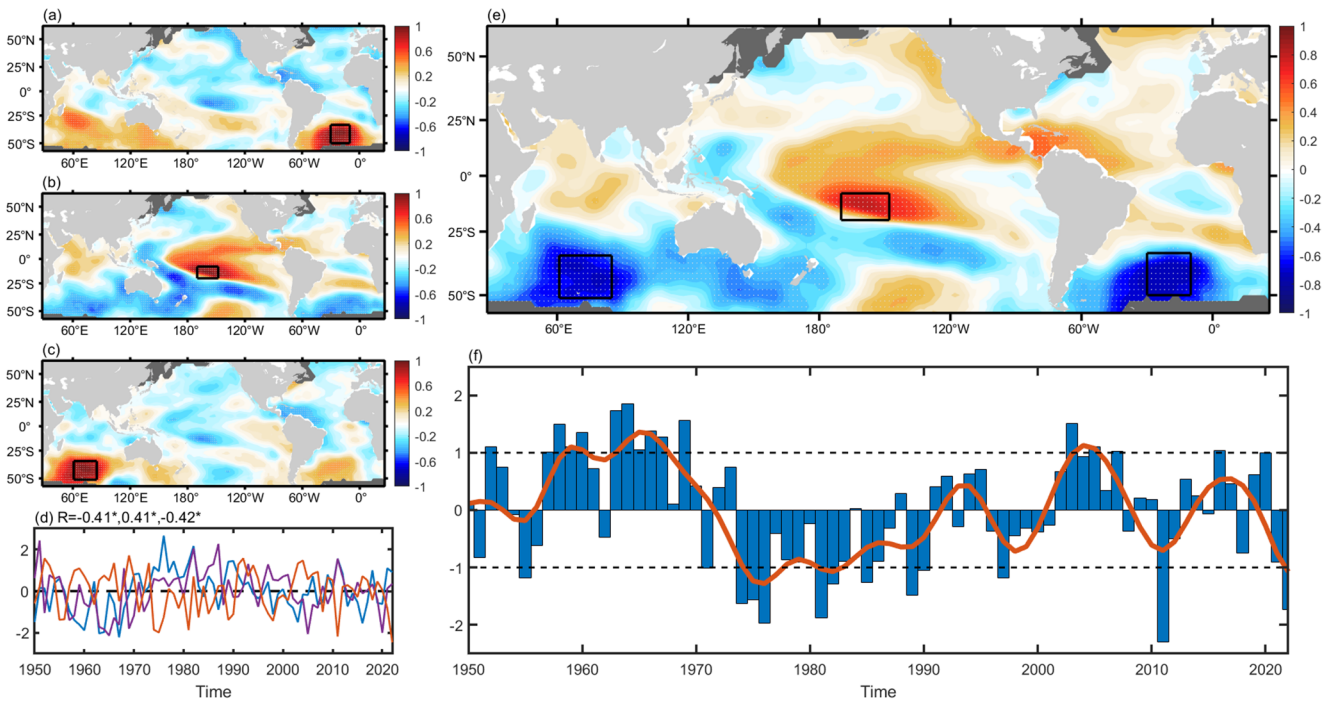

Fig. 14 **a** As in Fig. 2a, but in the South Atlantic (10°–30°W, 34°–50°S). **b** As in **a**, but in the tropical South Pacific (148°–170°W, 8°–20°S). **c** As in **a**, but in the South Indian Ocean (62°–84°E, 36°–50°S). Dots indicate the correlations significant at the 99% confidence level. **d** As in Fig. 2c, but with the blue line representing the South Atlantic (boxed region in **a**), the red line representing the tropical South Pacific (boxed region in **b**), the purple line representing the South Indian Ocean (boxed region in **c**). **e** As in Fig. 2d, but between the SHT index and the global SST anomalies. **f** As in Fig. 2e, but of the standardized SHT index

phase around 1970. In contrast, from 1990 to 2022, it exhibits several phase transitions.

Table 1 reveals significant correlations between SHT and three known modes, including the NPMM, AMV and SSTID. Figure 15 presents the partial correlation maps of SHT after removing the signals from these mode indices. Notably, the tripole pattern remains statistically significant and maintains its spatial position. The SAM is the dominant mode of extratropical Southern Hemisphere weather and climate variability, exerting important influences on Southern Hemisphere temperature, precipitation, and ocean circulation (Purich et al. 2026). We examined the relationship between the SHT and the SAM, finding that their correlation coefficient is not significant ($R = -0.23$). Furthermore, the SAM exhibits a significant upward trend, which is not observed in the SHT (Fig. S17b). Figure S17a shows the correlation map between the SHT index and global SST after removing the SAM signal. The key sea-area signals of the SHT remain pronounced, and the Southern Hemisphere SST still displays a "negative-positive-negative" tripole pattern. These results indicate that the SHT is distinct from these modes and exists as a relatively independent IBT.

8 Summary and discussion

This study employs the IBT analysis proposed by Han and Li (2023) to provide a detailed and comprehensive characterization of the global distribution of simultaneous IBTs across ocean basins in the annual mean SST field, thereby advancing our understanding on inter-basin linkages and interactions across ocean basins. The reproducibility of this result has been validated in another independent dataset.

Using this approach, we identify 11 distinct IBTs. These include two previously recognized and studied patterns—the BCS and SASI—along with nine new potential IBTs. Among the new IBTs, two represent remote linkages between known climate modes and distant ocean basins: specifically, the connection of the IOB with the North Atlantic, and that of the PDO with the Mediterranean Sea. The remaining seven IBTs include the BBSA, NASI, and CSSI between the Indian and Atlantic Oceans; NPSA and SPSA between the Pacific and Atlantic Oceans; NTIP between the Indian and Pacific Oceans; and hemispheric-scale SHT. We characterize the spatiotemporal features of these seven IBTs, thereby establishing a foundation for further investigation into their physical mechanisms and climatic impacts. To further verify the robustness of these seven IBTs, we employed coherence spectral analysis and applied the posteriori statistical test method (Madden and Julian 1971). At a posteriori significance level of 3% (prior significance level of 0.25%), the coherence spectra between the time series of the two key sea areas for each IBT shows 1–3 significant peaks on interannual to decadal scale (Fig. S18). For the SHT, significant peaks around 2–3 years are observed in the pairwise coherence spectra of its three key sea areas (Fig. S18). Meanwhile, we computed the indices of these seven IBTs using another SST dataset, and obtained nearly identical results (Fig. S19).

We assess the relationships and distinctions between these seven IBTs and several known oceanic modes. While certain established modes exhibit notable correlations with these IBTs, none can adequately explain them. To further substantiate these findings, we statistically analyzed the co-occurrence frequency between these seven IBTs and several known climate modes (Saji et al. 1999). Previous studies indicate that ENSO exhibits diverse anomaly centers,

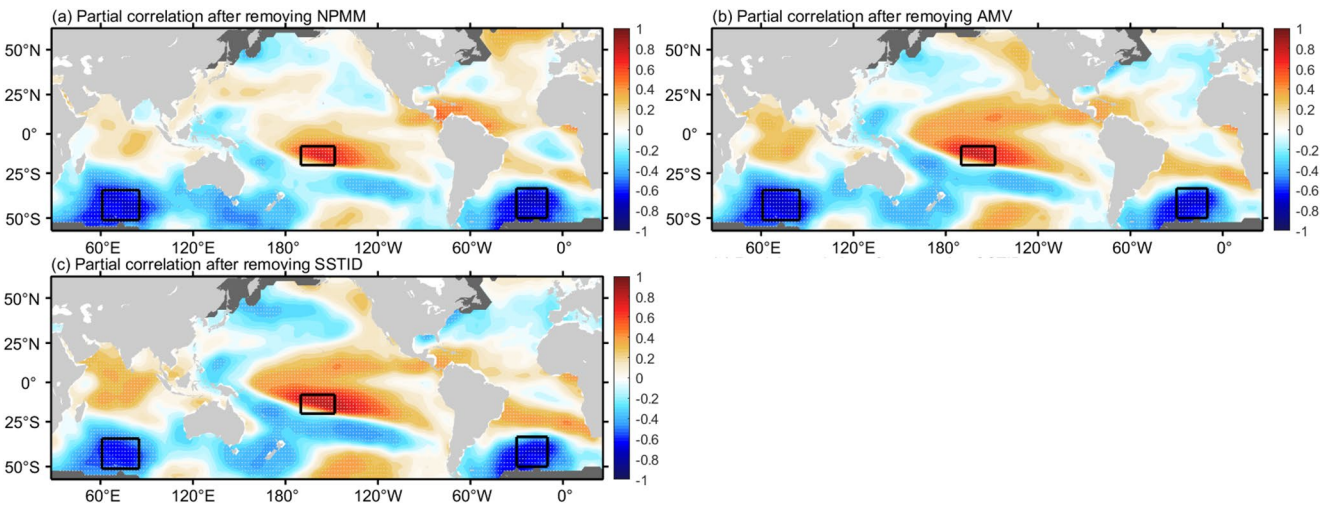

Fig. 15 Partial correlation maps between the global SST anomalies and SHT index after removing the signals of several known modes. **a** NPMM. **b** AMV **c** SSTID. Dots indicate the correlations significant at the 99% confidence level

Table 2 The co-occurrence frequency matrix between IBTs and some known modes

	BBSA (%)	NASI (%)	CSSI (%)	SPSA (%)	NPSA (%)	NTIP (%)	SHT (%)
PDO	42.9	21.7	30.0	42.3	40.9	29.4	23.1
NPMM	10.3	26.1	15.0	26.9	18.2	29.4	34.6
SPMM	38.1	17.4	25.0	38.5	36.4	52.9	26.9
IOB	52.4	26.1	15.0	23.1	31.8	29.4	15.4
IOD	9.5	17.4	25.0	23.1	18.2	29.4	23.1
AMV	23.8	52.2	50.0	23.1	13.6	35.3	42.3
Atlantic Niño	28.6	30.4	15.0	23.1	27.3	17.7	23.1
NTA	14.3	13.0	45.0	23.1	9.1	11.8	19.2
SSTID	38.1	47.8	35.0	26.9	36.4	29.4	34.6
Niño3.4	33.3	30.4	25.0	38.5	27.3	29.4	38.5
E-Index	19.1	13.4	10.0	15.4	22.7	41.2	38.5
C-Index	23.8	21.7	30.0	38.5	27.3	23.5	19.2

Table 3 The temporal correlation matrix for the seven IBTs indices

	BBSA	NASI	CSSI	SPSA	NPSA	NTIP	SHT
BBSA	1	−0.18	0.06	−0.14	−0.57*	0.61*	0.14
NASI		1	0.43*	0.28	0.17	−0.11	0.39*
CSSI			1	−0.16	−0.01	0.02	0.55*
SPSA				1	0.24	−0.31*	−0.32*
NPSA					1	−0.55*	−0.02
NTIP						1	−0.08
SHT							1

The asterisks indicate significant values at the 99% confidence level

referred to as EP-ENSO and CP-ENSO regimes, respectively. Moreover, their corresponding indices (E-index and C-index) are orthogonal (Takahashi et al. 2011; Geng et al. 2022). Therefore, we discuss them separately. Based on ± 1 standard deviation, positive and negative phase of the IBTs and known modes events are determined. The results show substantial differences in occurrence frequency between most IBTs and the known modes. Only the BBSA with the IOB, the NASI with the AMV, the CSSI with the AMV, and the NTIP with the SPMM exhibited co-occurrence frequencies exceeding 50% (Table 2). Taking the BBSA and IOB as an example, from 1950 to 2022, 10 positive BBSA events and 11 negative BBSA events were identified. Among these, 5 positive events co-occurred with positive IOB events, and 6 negative events co-occurred with negative IOB events. The substantial mismatch in their occurrence years also indicates a distinction between the two. Similarly, other IBTs show notable differences from these known modes.

Then, are these seven IBTs relatively independent of each other, or do they represent different phases or manifestations of a same larger oscillatory system? We calculated the correlation coefficients among the seven IBTs (Table 3). The results show that most correlations between the IBTs are weak, indicating their statistical independence. Although eight pairs exhibit relatively higher correlations that reach the 99% confidence level, this alone does not confirm that they represent the same mode. This is similar to the five major teleconnection patterns identified by Wallace and Gutzler (1981), which exhibit significant interrelationships while remaining relatively independent of one another. Therefore, we further employed partial regression to verify their independence (the relationships among BBSA, NPSA, and NTIP have already been discussed in Sect. 3.1). Taking NASI and CSSI as an example, we found that after mutually removing the signals of the other's index, the original signals in the two key sea areas of each IBT remain significant, further confirming their relative independence (Fig. S20a and b). The same holds for the remaining five highly correlated pairs (Fig. S20). This analysis demonstrates that these IBTs are not different phases or manifestations of the same oscillatory system but represent relatively independent cross-basin teleconnection signals. This also suggests that these IBTs may reflect distinct and independent inter-basin linkages between ocean basins, likely driven by different physical mechanisms.

The fundamental causes and dynamic mechanisms underlying these IBTs remain unclear. However, as mentioned earlier, these IBTs are spatially distributed across different ocean areas, implying considerable differences in the local dynamical processes involved. Temporally, they also exhibit substantial variations from interannual to decadal timescales. These indicate that it is difficult to explain all IBTs in a single unified dynamical framework. Each IBT may involve distinct atmospheric or oceanic processes. For instance, the NTIP might be modulated by the WPSH above it (Wang et al. 2013), while the SPSA could link its two key

sea areas via cross-equatorial Rossby waves (Li et al. 2019a, b). A thorough investigation into the physical mechanisms of each IBT is beyond the scope of this paper, and each IBT requires detailed, individual study in future work. Other issues also warrant further investigation. Firstly, Ocean currents transport heat and influence SST patterns (Feng et al. 2013). Previous studies have identified teleconnections between currents in different ocean basins (Kohyama et al. 2021a; Han and Li 2023), raising the question of whether the IBTs identified here reflect such inter-basin current linkages. Secondly, the ABCD mode previously identified in the boreal winter SST field exhibits a much weaker signal in the annual mean SST field, making it difficult to effectively identify. This suggests that some IBTs display distinct seasonal preferences, highlighting the necessity of applying IBT analysis in different seasonal SST fields for further investigation. Moreover, the synchronization characteristics between the Brazil Current and the Agulhas Return Current are not well captured in the annual mean SST field, indicating the importance of applying the IBT analysis to SST field across various time scales to study inter-basin linkages. Thirdly, detailed analysis is required to assess their effects on regional and global climate systems. Finally, the IBTs we observe merely represent simultaneous linkages. Considering the time lags in the propagation of climatic signals, significant lead-lag relationships also exist across different ocean basins. For example, as mentioned in the introduction section, a lead-lag relationship exists between the North Pacific SST variability and AMV, as well as other linkages such as the IOD triggering an Atlantic Niño with a 3–5 month lag (Zhang and Han 2021). Therefore, it is necessary to apply the IBT analysis to investigate lead-lag interactions among ocean basins.

Supplementary Information The online version contains supplementary material available at https://doi.org/10.1007/s00382-026-08145-9.

Acknowledgements Thanks for the helpful discussions and suggestions from Mr. Hongyuan Zhao, Mr. Ning Wang, Mr. Yifeng Wang and Mr. Xinshang Zhang. This research was supported by the National Key R&D Program of China (2023YFF0805100) and Laoshan Laboratory (No.LSKJ202202600).

Author contributions JL conceived of the study and guided the research. DZ performed data analysis, generated the figures and wrote the original drafts. JL revised the manuscript. All authors contributed to the discussions, reviews and improvement of this paper.

Funding This research was supported by the National Key R&D Program of China (2023YFF0805100) and Laoshan Laboratory (No. LSKJ202202600).

Data availability The datasets analyzed during this study are publicly available from the following repositories: Sea surface temperature data: NOAA Extended Reconstructed SST Version 5 (ERSST v5) https://psl.noaa.gov/data/gridded/data.noaa.ersst.v5.html. Japan Meteorological Agency's Centennial in situ Observation-Based Estimates SST (COBE SST). https://psl.noaa.gov/data/gridded/data.cobe.html.

Declarations

Conflict of interest The authors have no relevant financial or non-financial interests to disclose.

References

An Q, Li J, Yang J (2024) Evaluation of sea surface temperature interhemispheric dipole in CMIP6 historical simulations. Clim Dyn 62:10347–10362. https://doi.org/10.1007/s00382-024-07455-0

Bingham C, Godfrey M, Tukey J (1967) Modern techniques of power spectrum estimation. IEEE Trans Audio Electroacoust 15(2):56–66. https://doi.org/10.1109/TAU.1967.1161895

Bjerknes J (1969) Atmospheric teleconnections from the equatorial Pacific. Mon Weather Rev 97:163–172. https://doi.org/10.1175/1520-0493(1969)097%3c0163:ATFTEP%3e2.3.CO;2

Cai W, Wu L, Lengaigne M et al (2019) Pantropical climate interactions. Science 363:eaav4236. https://doi.org/10.1126/science.aav4236

Chiang JCH, Vimont DJ (2004) Analogous Pacific and Atlantic meridional modes of tropical atmosphere–ocean variability. J Clim 17:4143–4158. https://doi.org/10.1175/JCLI4953.1

Czaja A, van der Vaart P, Marshall J (2002) A diagnostic study of the role of remote forcing in tropical Atlantic variability. J Clim 15:3280–3290. https://doi.org/10.1175/1520-0442(2002)015%3c3280:ADSOTR%3e2.0.CO;2

Ding R, Li J, Yang R et al (2020) On the differences between the South Pacific meridional and quadrupole modes. J Geophys Res Oceans 125:e2019JC015500. https://doi.org/10.1029/2019JC015500

Enfield DB, Mestas-Nuñez AM, Trimble PJ (2001) The Atlantic Multidecadal Oscillation and its relation to rainfall and river flows in the continental U.S. Geophys Res Lett 28:2077–2080. https://doi.org/10.1029/2000GL012745

Feng M, McPhaden M, Xie SP et al (2013) La Niña forces unprecedented Leeuwin Current warming in 2011. Sci Rep 3:1277. https://doi.org/10.1038/srep01277

Geng T, Cai W, Wu L, Santoso A, Wang G, Jing Z, Gan B, Yang Y, Li S, Wang S, Chen Z, McPhaden MJ (2022) Emergence of changing Central-Pacific and Eastern-Pacific El Niño-Southern Oscillation in a warming climate. Nat Commun 13:6616. https://doi.org/10.1038/s41467-022-33930-5

Gill AE (1982) Atmosphere-ocean dynamics. Academic Press, New York

Ha KJ, Chu JE, Lee JY, Yun KS (2017) Interbasin coupling between the tropical Indian and Pacific Ocean on interannual timescale: observation and CMIP5 reproduction. Clim Dyn 48:459–475. https://doi.org/10.1007/s00382-016-3087-6

Ham YG, Kug JS, Park JY et al (2013) Sea surface temperature in the north tropical Atlantic as a trigger for El Niño/Southern Oscillation events. Nat Geosci 6:112–116. https://doi.org/10.1038/ngeo1686

Han JH, Li J (2023) Discovery of a new inter-basin climate pattern: Australia boundary current dipole. Geophys Res Lett 50:e2022GL102715. https://doi.org/10.1029/2022GL102715

Huang B, Thorne PW, Banzon VF et al (2017) Extended reconstructed sea surface temperature, version 5 (ERSSTv5): upgrades, validations, and intercomparisons. J Clim 30:8179–8205. https://doi.org/10.1175/JCLI-D-16-0836.1

Ishii M, Shouji A, Sugimoto S, Matsumoto T (2005) Objective analyses of sea-surface temperature and marine meteorological variables for the 20th century using ICOADS and the Kobe Collection. Int J Climatol 25:865–879. https://doi.org/10.1002/joc.1169

Izumo T, Vialard J, Dayan H et al (2016) A simple estimation of equatorial Pacific response from windstress to untangle Indian Ocean Dipole and basin influences on El Niño. Clim Dyn 46:2247–2268. https://doi.org/10.1007/s00382-015-2700-4

Kerr RA (2000) A North Atlantic climate pacemaker for the centuries. Science 288:1984–1986. https://doi.org/10.1126/science.288.5473.1984

Klein SA, Soden BJ, Lau NC (1999) Remote sea surface temperature variations during ENSO: evidence for a tropical atmospheric bridge. J Clim 12:917–932. https://doi.org/10.1175/1520-0442(1999)012%3c0917:RSSTVD%3e2.0.CO;2

Kohyama T, Yamagami Y, Miura H, Kido S, Tatebe H, Watanabe M (2021a) The Gulf Stream and Kuroshio Current are synchronized. Science 374:341–346. https://doi.org/10.1126/science.abh3295

Kohyama T, Miura H, Kido S (2021b) Intensive variability extraction. SOLA 17:246–250

Li J, Zheng F, Sun C, Feng J, Wang J (2019a) Pathways of influence of the Northern Hemisphere mid-high latitudes on East Asian climate: a review. Adv Atmos Sci 36:902–921. https://doi.org/10.1007/s00376-019-8236-5

Li Y, Feng J, Li J, Hu A (2019b) Equatorial windows and barriers for stationary Rossby wave propagation. J Clim 32:6117–6135. https://doi.org/10.1175/JCLI-D-18-0722.1

Li J, Xie T, Tang X et al (2022) Influence of the NAO on wintertime surface air temperature over East Asia: multidecadal variability and decadal prediction. Adv Atmos Sci 39:625–642. https://doi.org/10.1007/s00376-021-1075-1

Madden RA, Julian PR (1971) Detection of a 40–50 day oscillation in the zonal wind in the tropical Pacific. J Atmos Sci 28:702–708. https://doi.org/10.1175/1520-0469(1971)028%3c0702:DOADOI%3e2.0.CO;2

Mantua NJ, Hare SR, Zhang Y et al (1997) A Pacific interdecadal climate oscillation with impacts on salmon production. Bull Am Meteorol Soc 78:1069–1080. https://doi.org/10.1175/1520-0477(1997)078%3c1069:APICOW%3e2.0.CO;2

Morioka Y, Taguchi B, Behera SK (2017) Eastward propagating decadal temperature variability in the South Atlantic and Indian Oceans. J Geophys Res Oceans 122:5611–5623. https://doi.org/10.1002/2017JC012706

Nan S, Li J (2003) The relationship between the summer precipitation in the Yangtze River valley and the boreal spring Southern Hemisphere annular mode. Geophys Res Lett 30:2266. https://doi.org/10.1029/2003GL018381

North GR, Bell TL, Cahalan RF, Moeng FJ (1982) Sampling errors in the estimation of empirical orthogonal functions. Mon Weather Rev 110:699–706. https://doi.org/10.1175/1520-0493(1982)110%3c0699:SEITEO%3e2.0.CO;2

Purich A, Arblaster JM, Boschat G et al (2026) Southern Annular Mode dynamics, projections and impacts in a changing climate. Nat Rev Earth Environ 7:24–42. https://doi.org/10.1038/s43017-025-00746-y

Richter I, Stuecker MF, Takahashi N et al (2022) Disentangling the North Pacific meridional mode from tropical Pacific variability. Npj Clim Atmos Sci 5:94. https://doi.org/10.1038/s41612-022-00317-8

Saji NH, Goswami BN, Vinayachandran PN, Yamagata T (1999) A dipole mode in the tropical Indian Ocean. Nature 401:360–363. https://doi.org/10.1038/43854

Sun C, Li J, Jin FF, Ding R (2013) Sea surface temperature inter-hemispheric dipole and its relation to tropical precipitation. Environ Res Lett 8:044006. https://doi.org/10.1088/1748-9326/8/4/044006

Sutton RT, Hodson DLR (2005) Atlantic Ocean forcing of North American and European summer climate. Science 309:115–118. https://doi.org/10.1126/science.1109496

Takahashi K, Montecinos A, Goubanova K, Dewitte B (2011) ENSO regimes: reinterpreting the canonical and Modoki El Niño. Geophys Res Lett 38:L10704. https://doi.org/10.1029/2011GL047364

Wallace JM, Gutzler DS (1981) Teleconnections in the geopotential height field during the Northern Hemisphere winter. Mon Weather Rev 109:784–812. https://doi.org/10.1175/1520-0493(1981)109%3c0784:TITGHF%3e2.0.CO;2

Wang C (2019) Three-ocean interactions and climate variability: a review and perspective. Clim Dyn 53:5119–5136. https://doi.org/10.1007/s00382-019-04930-x

Wang B, Xiang B, Lee JY (2013) Subtropical high predictability establishes a promising way for monsoon and tropical storm predictions. Proc Natl Acad Sci U S A 110:2718–2722. https://doi.org/10.1073/pnas.1214626110

Xue J, Sun C, Li J, Mao J (2018) South Atlantic forced multidecadal teleconnection to the midlatitude south Indian Ocean. Geophys Res Lett 45:8480–8489. https://doi.org/10.1029/2018GL078990

Yang JL, Liu QY, Xie SP et al (2007) Impact of the Indian Ocean SST basin mode on the Asian summer monsoon. Geophys Res Lett 34:L02708. https://doi.org/10.1029/2006GL028571

Zebiak SE (1993) Air-sea interaction in the equatorial Atlantic region. J Clim 6:1567–1586. https://doi.org/10.1175/1520-0442(1993)006%3c1567:AIITEA%3e2.0.CO;2

Zhang R, Delworth TL (2007) Impact of the Atlantic multidecadal oscillation on North Pacific climate variability. Geophys Res Lett 34:L23708. https://doi.org/10.1029/2007GL031601

Zhang L, Han W (2021) Indian Ocean Dipole leads to Atlantic Niño. Nat Commun 12:5952. https://doi.org/10.1038/s41467-021-26223-w

Zhang H, Clement A, Di Nezio P (2014) The South Pacific meridional mode: a mechanism for ENSO-like variability. J Clim 27:769–783. https://doi.org/10.1175/JCLI-D-13-00082.1

Zhang L, Han W, Karnauskas KB et al (2023) Emergence of the Central Atlantic Niño. Sci Adv 9:eadi5507. https://doi.org/10.1126/sciadv.adi5507

Zheng XT, Xie SP, Liu QY (2011) Response of the Indian Ocean basin mode and its capacitor effect to global warming. J Clim 24:6146–6164. https://doi.org/10.1175/2011JCLI4169.1